PHOTONICS Research

Higher-order exceptional points in waveguide-coupled microcavities: perturbation induced frequency splitting and mode patterns

JULIUS KULLIG,[1,*] ORCID DANIEL GROM,[1,3] SEBASTIAN KLEMBT,[2] AND JAN WIERSIG[1] ORCID

[1]*Institut für Physik, Otto-von-Guericke-Universität Magdeburg, 39106 Magdeburg, Germany*
[2]*Technische Physik and Würzburg-Dresden Cluster of Excellence ct.qmat, Physikalisches Institut and Wilhelm-Conrad-Röntgen-Research Center for Complex Material Systems, Am Hubland, University of Würzburg, 97070 Würzburg, Germany*
[3]*e-mail: daniel.grom@ovgu.de*
Corresponding author: julius.kullig@ovgu.de

Exceptional points are degeneracies in the spectrum of non-Hermitian open systems where at least two eigenfrequencies and simultaneously the corresponding eigenstates of the Hamiltonian coalesce. Especially, the robust construction of higher-order exceptional points with more than two degenerate eigenfrequencies and eigenstates is challenging but yet worthwhile for applications. In this paper, we reconsider the formation of higher-order exceptional points through waveguide-coupled microring cavities and asymmetric backscattering. In this context, we demonstrate the influence of perturbations on the frequency splitting of the system. To generate higher-order exceptional points in a simple and robust way, a mirror-induced asymmetric backscattering approach is used. In addition to the exceptional-point enhanced sensing capabilities of such systems, also a cavity-selective sensitivity is achieved for particle sensing. The results are motivated by an effective Hamiltonian description and verified by full numerical simulations of the dielectric structure. © 2023 Chinese Laser Press

1. INTRODUCTION

In contrast to closed Hermitian systems, open non-Hermitian systems can feature an interesting type of degeneracies where not only the eigenvalues or frequencies but simultaneously also the corresponding eigenstates or modes of the Hamiltonian coalesce [1–3]. This phenomenon typically occurs at specific points in the parameter space, which are therefore called exceptional points (EPs). In the past years, the research on EPs has been growing enormously especially but not exclusively in optics and photonics [4–7]. A plethora of interesting phenomena and applications arise around EPs, some of which are EP-based sensing [8–15], loss-induced revival of lasing [16], orbital angular momentum lasers [17], single-mode lasing [18], topological defect engineering [19], topologically curved microcavities [20], time-symmetry breaking in cavity quantum electrodynamics systems [21], electromagnetically induced transparency [22], synthetic dimensions with anti-PT symmetry [23], or optical amplifiers [24].

A key challenge is the generation of higher-order EPs where $n > 2$ eigenstates and eigenvectors coalesce. Such EPs of order n (EP_n) have a characteristic nth root topology of their complex eigenvalues in parameter space, which makes them exceedingly suited for sensing applications as a small perturbation

generically results in a sizable response of the frequencies due to the steep slope of the nth root at the EP [25].

On the other hand, the extreme sensitivity makes the realization of a system at an EP_n challenging and often includes a delicate fine tuning of parameters. For example, Hodaei *et al.* [11] realized an enhanced frequency splitting at an EP_3 with three optical ring resonators with fine-tuned gain and loss. In Ref. [26], the authors proposed an optical microcavity with a precisely tuned boundary shape to generate an EP_4. Other systems with high-order EPs suggested are optomechanical systems [27,28], resonators with spin–orbit interaction [29], parity–time symmetric cavities [11,30,31], waveguide (WG)-coupled refractive index tuned cavities [32], WG-coupled cavities with optical isolators [33], and recently coupled cavities with tuned asymmetric auxiliary WG elements [34].

A solution for the robust fabrication of an EP_2 has been proposed in terms of exceptional surfaces [35–37], whereby fabrication tolerances represent non-generic perturbations that do not drive the system away from the EP whereas, e.g., a test particle (TP) does drive the system away from the EP and, therefore, leads to an EP-enhanced frequency splitting. Zhong *et al.* [35] proposed an exceptional surface in an elegant way by coupling a microring cavity to a WG with a mirror at the end. Therefore, clockwise (CW) and counterclockwise

(CCW) propagating waves in the microring are coupled via asymmetric backscattering [38] such that an EP_2 is generated. The existence of the EP_2 is independent from fabrication parameters like the precise edge-to-edge distance between the WG and microring but shows an EP-enhanced sensing of a TP.

Furthermore, Wang *et al.* [32] showed that already two (three) microring cavities coupled by a single WG form two EP_2s (EP_3s). They additionally increase the order of the EP to four (six) via a sophisticated fine tuning of the refractive index profile of the individual microrings.

In this paper, we build on the approaches by Zhong *et al.* [35] and Wang *et al.* [32] and develop them further. In contrast to their works, we construct higher-order EPs with an easy-to-realize and robust fabrication scheme where a fine tuning of parameters is not necessary. Our proposed setup is supposed to work at room temperature and is scalable in size. In particular, we investigate two setups of N WG-coupled microring cavities that form an EP of order $2N$ by placing a mirror at one end of a WG. One of these setups with $N = 3$ cavities and the corresponding eigenmodes of an EP_6 is illustrated in the front of Fig. 1. The analog setup without a mirror is visualized in the background. In contrast to the proposed scheme, the mirrorless setup is at two EP_3s with similar eigenmodes. We show that systems consisting of WG-coupled microring cavities with mirror-induced asymmetric backscattering enable an EP-enhanced particle sensing with an interesting and potentially useful cavity-selective scaling of the sensitivity.

Within coupled-mode theory, an effective Hamiltonian as a $2N \times 2N$ matrix is constructed, which allows for an intuitive understanding of the EP formation. In addition, the effective Hamiltonian description has an excellent agreement with the numerical finite-element method (FEM) simulations of the system including the complex eigenfrequencies and the reflection spectra of the system perturbed by a TP.

The paper is organized as follows. In Section 2, the system of two WG-coupled cavities is revised. In Section 3, the two schemes for the higher-order EP construction are discussed. A summary is given in Section 4.
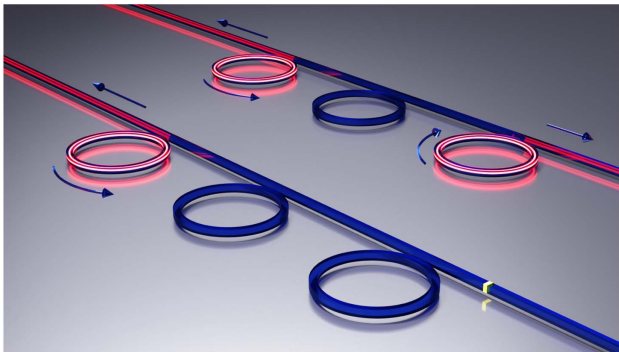
Fig. 1. Illustration of different setups with the corresponding eigenmodes for the realization of higher-order EPs. In the front is an example for an EP_6 realized with the proposed scheme consisting of three WG-coupled microrings and a gold mirror. The setup in the background with three WG-coupled microrings is at two EP_3s. The arrows show the traveling direction of the confined light.

2. TWO WG-COUPLED MICRORING CAVITIES

First, some preliminary considerations using a matrix model are in order. A single microring cavity is assumed, which is coupled to a WG. This situation is very well described by an effective two-mode Hamiltonian H_0 in the basis of CCW and CW propagating waves as

$$H_0 = \begin{pmatrix} \Omega & D \\ D & \Omega \end{pmatrix}, \qquad (1)$$

where Ω is the complex frequency of the CCW and CW waves. The complex off-diagonal elements D reflect the small symmetric coupling between CW and CCW waves due to the weak backreflections at the WG. Adding a small TP to the cavity is typically described by a perturbation matrix. An approach for the design of such a perturbation matrix for an isolated microdisk perturbed by two TPs is given in Ref. [39]. Here, we interpret the WG already as one of the TPs leading to the matrix in Eq. (1). Thus, adding a TP to the WG-perturbed cavity adds a perturbation matrix of the following form:

$$H_{TP} = \begin{pmatrix} V + U & (V - U)e^{-i2m\phi_{TP}} \\ (V - U)e^{i2m\phi_{TP}} & V + U \end{pmatrix}, \qquad (2)$$

where m is the azimuthal mode number of the mode to be perturbed and ϕ_{TP} is the angle between the WG and the TP. The complex parameters V and U include the perturbation strength induced by the TP. Usually $|U|$ is much smaller than $|V|$. For small perturbations, i.e., small radii r_{TP} of the TP, the parameter U is negligible. Therefore,

$$H_{TP}(\epsilon) \approx \epsilon \begin{pmatrix} 1 & e^{-i2m\phi_{TP}} \\ e^{i2m\phi_{TP}} & 1 \end{pmatrix}, \qquad (3)$$

where the perturbation strength $\epsilon \equiv V$ scales with r_{TP}^2. This statement is in agreement with Zhong *et al.* [30] and further reviewed in Appendix A.

Hence, the eigenvalues Ω_i of the perturbed system $H(\epsilon) = H_0 + H_{TP}(\epsilon)$ have a splitting,

$$\Delta\Omega = |\Omega_1 - \Omega_2| = 2|\sqrt{D^2 + 2D\epsilon \cos(2m\phi_{TP}) + \epsilon^2}|, \qquad (4)$$

which increases linearly in $|\epsilon|$ for $|D| \ll |\epsilon|$. Note that this is the typical observation as D is often negligibly small.

The extension of the matrix model to a system with two identical microring cavities coupled via a WG is straightforward; see Fig. 2(a) and Ref. [32]. In the basis of CCW/CW waves of the left and CCW/CW waves of the right microring, the effective Hamiltonian reads

$$H_0 = \begin{pmatrix} \Omega & D & A & 0 \\ D & \Omega & 0 & 0 \\ 0 & 0 & \Omega & D \\ 0 & A & D & \Omega \end{pmatrix}. \qquad (5)$$

Due to the spatial symmetry of the WG-microring system, the complex coupling parameter A is the same for CCW waves from the right to the left cavity and for CW waves from the left to the right cavity. It is assumed that the symmetric internal backscattering D at the WG is small compared to the directional coupling from one cavity to the other implying $|A| \gg |D|$ holds. In particular, this condition is fulfilled close to the critical coupling regime. For the idealized case $D = 0$,

the effective Hamiltonian [Eq. (5)] has two EP$_2$s with eigenvalue Ω and associated eigenstates $(1, 0, 0, \pm1)^T$. Thus, two microring cavities coupled via a WG realize in a good approximation an EP; see Ref. [32].

If a perturbation of a higher-order EP$_N$ is considered, the N frequencies Ω_i diverge along the Riemann sheets of an Nth-order root. Therefore, the generalization of the splitting $\Delta\Omega$ from Eq. (4) to more than two frequencies is not straightforward. In this paper, we use the convenient definition,

$$\Delta\Omega = \max_{i,j}|\Omega_i - \Omega_j|, \qquad (6)$$

which is the maximal distance in the complex plane between two frequencies emerging from the EP for a given perturbation; see Fig. 3 for an illustration. The definition is consistent with Eq. (4) and captures the characteristic behavior of the frequencies around an EP$_N$.

For the purpose of TP-sensing, it needs to be distinguished at which cavity a TP is placed. The perturbation matrix for a TP at the left or at the right cavity can be constructed via $H^{(1)}_{TP}(\epsilon) = H_{TP}(\epsilon) \oplus 0_{2,2}$ or $H^{(2)}_{TP}(\epsilon) = 0_{2,2} \oplus H_{TP}(\epsilon)$, respectively. Thus, the effective Hamiltonian of the system with one TP at the left cavity reads

$$H^{(1)}(\epsilon) = H_0 + H^{(1)}_{TP}(\epsilon), \qquad (7)$$

with H_0 from Eq. (5). In contrast, placing two identical TPs at each cavity leads to the effective Hamiltonian,

$$H^{(1+2)}(\epsilon) = H_0 + H^{(1)}_{TP}(\epsilon) + H^{(2)}_{TP}(\epsilon). \qquad (8)$$

These two scenarios lead to a different behavior of the splitting $\Delta\Omega$ as shown in Fig. 2. For this idealized case with $D = 0$ [see Fig. 2(b)], the system shows the expected square-root scaling of the splitting $\Delta\Omega$ at an EP$_2$ if it is perturbed by two identical TPs, one at each cavity. A closer look at the analytic solution of the eigenvalue problem with the Hamiltonian $H^{(1+2)}$ for the exemplary parameters $(D, m, \phi_{TP}) = (0, 20, \pi/2)$ reveals that

for $\sqrt{|\epsilon/A|} \ll 1$ the eigenstates are $\sim(1, 0, 0, \pm1)^T$ with a dominant square-root scaling of the corresponding eigenvalues. If $\sqrt{|\epsilon/A|} \ll 1$ is not fulfilled, the linear scaling of the eigenvalues is dominant. The transition from a square-root to a linear scaling of the splitting is only present for symmetric perturbations of both cavities. Placing a single TP solely at the left cavity represents a non-generic perturbation [25] within which only a linear scaling of the frequency splitting can be observed for $D = 0$ over the whole ϵ range. To understand this behavior, the solution of the eigenvalue problem with $H^{(1)}$ for parameters $(D, m, \phi_{TP}) = (0, 20, \pi/2)$ in Eq. (7) is useful. It shows that, through the perturbation, an EP$_3$ with eigenvalue Ω and eigenstate $(0, 0, 0, 1)^T$ independent from ϵ is formed. This means that the perturbation forms an EP$_3$ and moves the system along a corresponding exceptional surface [35,36] only changing the remaining eigenvalue $\Omega + 2\epsilon$ and eigenstate $(2\epsilon/A, 2\epsilon/A, 0, 1)^T$. Remarkably, if $2\epsilon/A$ is chosen small but still finite to break the symmetry, the eigenstates approximately coalesce to $\sim(0, 0, 0, 1)^T$, which indicates that the system is close to an EP$_4$ in parameter space.

For small but finite $D \neq 0$, interesting differences can be observed as shown in Fig. 2(c). One of the differences is the quartic-root scaling of the splitting $\Delta\Omega$ by placing a TP at the left cavity. In order to get an understanding for the observation, the matrix related to the parameter D can be apprehended as another perturbation. The combination of the ϵ and D perturbation leads the system being near an EP$_4$ even though the system itself without TP only supports two EP$_2$s. The finite ϵ and D in parallel excite the quartic-root scaling the most for a parameter range around $\epsilon \approx 10^{-9}, ..., 10^{-6}$. Note that this quartic-root, however, does not lead to an increased sensitivity as splitting for $H^{(1)}$ is smaller than the splitting for $H^{(1+2)}$; see Fig. 2(c).

As mentioned before, if $2\epsilon/A \ll 1$ is not fulfilled, the system is not close enough to an EP$_4$ in the parameter space; therefore, the linear scaling of the splitting becomes dominant. For $\epsilon \ll |D|$, the TP-induced perturbation is negligible compared to the small symmetric coupling D. Therefore, the observed saturation in Fig. 2(c) for small perturbation strength ϵ occurs. It is remarkable that the saturation value in $\Delta\Omega$ is orders of magnitudes larger than $|D|$ itself, whereas in the single-cavity case it is of the order of $|D|$. Here, the analytic solution of the eigenvalue problem with H_0 in Eq. (5) can provide an explanation: the eigenvalues are $\Omega \pm \sqrt{D^2 + DA}$ and $\Omega \pm \sqrt{D^2 - DA}$. Thus, for small $|D| \ll |A|$, the splitting $\Delta\Omega$ is of the order $\sqrt{|D|}$, i.e., the square root leads to the differences in magnitudes for the saturation values. For the case with two identical TPs on each cavity, the difference between Figs. 3(b) and 3(c) is the saturation effect for negligibly small TPs.

As will be discussed in the next section, already an infinitesimal small, asymmetric coupling between CCW and CW waves in the form of a single TP at one cavity could lead to the formation of a higher-order EP. However, the scaling of the frequency splitting $\Delta\Omega$ of the system is strongly related to the perturbation. In the example above, it is illustrated how the interaction of two perturbations, namely ϵ and D, can lead to an interesting scaling behavior of $\Delta\Omega$.
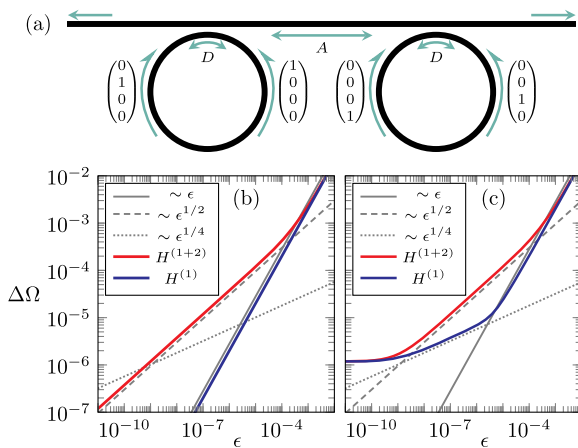
Fig. 2. (a) Illustration of two WG-coupled microrings. The WG is infinitely long without backscattering as indicated by the outward pointing arrows. (b), (c) Frequency splitting $\Delta\Omega$ for the matrix model of two WG-coupled microrings that are perturbed by TPs according to Eqs. (7) and (8). The parameters are $\Omega = 8.31 - 3.5 \times 10^{-4}i$, $A = 3.5 \times 10^{-4}$, $m = 20$, $\phi_{TP} = \pi/2$, and $\epsilon \in \mathbb{R}^+$. In (b) $D = 0$; in (c) $D = 10^{-9}$. Gray solid, dashed, and dotted lines serve as guides to the eye for the respective scaling.
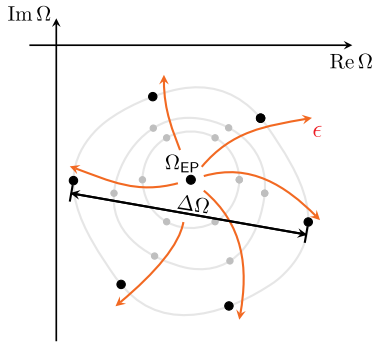
Fig. 3. Illustration of the perturbation-induced splitting around an EP_6 with frequency Ω_{EP}. For an increasing perturbation strength ϵ the complex frequencies Ω_i (dots) diverge from the EP. The splitting $\Delta\Omega$ is defined via Eq. (6) as the largest distance between two of the six frequencies for a given perturbation.

Next, a numerical simulation to verify the matrix model of the WG-coupled cavities is in order. Therefore, the FEM solver COMSOL Multiphysics [40] is used to find solutions of the mode equation,

$$(\Delta + n^2 k^2)\psi(x, y) = 0, \qquad (9)$$

for the quasi-two-dimensional geometry of the WG-coupled microrings; $\Omega = kR$ is the dimensionless complex frequency, k is the complex wavenumber, and n is the effective refractive index. In the simulation, we specify transverse magnetic polarization where ψ represents the z component of the electric field. The outer radius of the mircorings is set to $R = 10$ μm, and the width of the microrings is $R_w = 0.13R$, the same as the width of the WG h_{wg}. The edge-to-edge space between the microring and WG is $s = 0.133R$, and the edge-to-edge distance between the two rings is $d = 1.6R$. The refractive index of the microrings and WG is $n = 3.1$, and in the surrounding n is set to unity. For this setup, four quasi-degenerate modes with $\Omega_{1-4} \approx 8.3126 - 3.5 \times 10^{-4} i$ can be calculated numerically. The perturbation is simulated via TPs with variable radii r_{TP} and fixed refractive index $n_{TP} = 1.5$. The TPs are placed with an angle $\phi_{TP} = 0.4\pi$ and a fixed edge-to-edge distance $d_{TP} = 0.01R$ to the microring. From now on, the perturbation strength is defined as $\epsilon \equiv (r_{TP}/R)^2$. As shown in Fig. 4, the results from the FEM simulation are in very good agreement
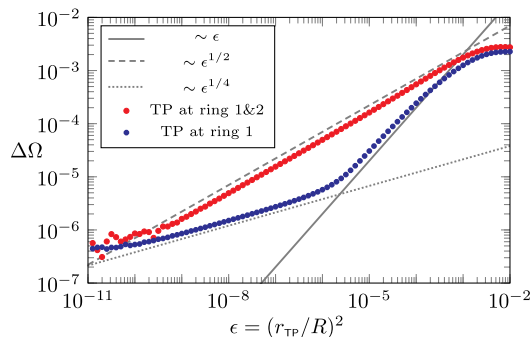
Fig. 4. Frequency splitting $\Delta\Omega$ [Eq. (6)] for two WG-coupled micoring cavities calculated with FEM simulations.
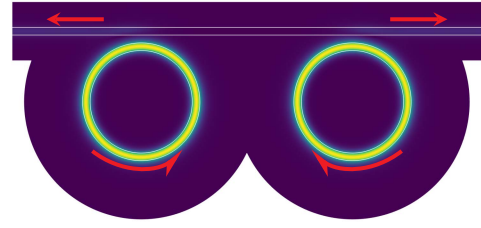
Fig. 5. Mode pattern $|\psi|$ for one of the four modes with $\Omega \approx 8.3126 - 3.5 \times 10^{-4} i$ in two WG-coupled microring cavities. Red arrows indicate the propagation direction of the field. The color-map in the simulated domain ranges from blue to yellow.

with the matrix model. In particular, the correct saturation for $\epsilon \to 0$ is observed as well as the scaling in the intermediate regime with $\epsilon^{1/4}$ or $\epsilon^{1/2}$. For larger $\epsilon \gtrsim 10^{-3}$, deviations from the matrix model arise. This is, however, expected as such a relatively large TP is no longer a localized perturbation to a microring, which is assumed in the perturbation matrix H_{TP} in Eq. (2).

For the WG-coupled cavities without TP, one of the four mode patterns $|\psi|$ is shown in Fig. 5. Note that the computational domain is adjusted to the geometry for all the simulated structures in the manuscript, which reduces the FEM grid by 10 to 25 percent compared to a comprising rectangular domain. In the mode pattern in Fig. 5, a finite $D \neq 0$ does not lead to a deviation from the idealized case $D = 0$ that can be observed by eyes. Thus, all four mode patterns look almost identical and consist of a CCW wave in the left ring and a CW wave in the right ring, which is consistently described by the two eigenstates $(1, 0, 0, \pm 1)$ of the Hamiltonian H_0 from Eq. (5) for $D = 0$.

It should be noted that the mechanisms leading to a finite backscattering D can be diverse. One is the already mentioned backscattering at the WG. In a realistic experimental implementation, the backscattering might also arise from fabrication tolerances and sidewall roughness. But even in the full numerical simulations, a finite simulation domain, a finite FEM mesh, or even computations with machine precision could lead to a finite D [31]. The latter seems negligibly small as the machine precision is of the order 10^{-16}. However, a naïve estimate shows that at an EP_4 this could lead to an induced splitting, $\Delta\Omega \sim \sqrt[4]{10^{-16}} = 10^{-4}$.

3. CONSTRUCTION OF HIGHER-ORDER EPS WITH WG-COUPLED CAVITIES

Previous works in Ref. [35] have demonstrated that a single cavity can be tuned into an EP_2 by coupling it to a WG with a mirror on one end as such a mirror leads to a fully asymmetric coupling between CW and CCW waves in the microring. In this section, we construct systems of N microring cavities that exhibit an EP of order $2N$. In particular, we discuss two implementations: (i) N cavities that are all coupled to the same WG [32], which has a mirror at one side, and (ii) N cavities that are coupled via $N + 1$ WGs [41], where only one WG has a mirror at the end. Both implementations have in common that the WG introduces a directional coupling between the
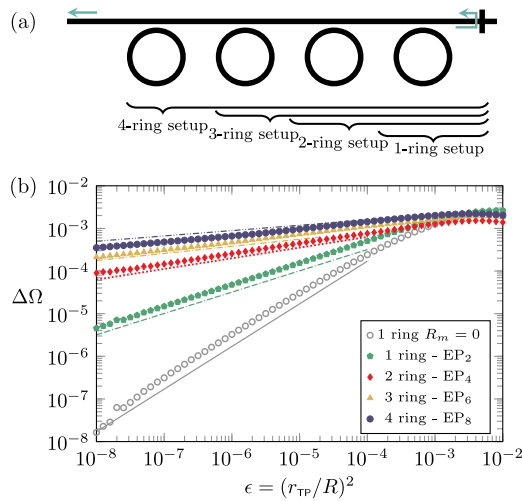
cavities as, e.g., a CCW mode in a cavity only couples to the CW or the CCW mode of the next cavity but not to both CW and CCW. Then the mirror at the WG end introduces an asymmetric coupling between CCW and CW waves.

Note that a recent publication by Liu *et al.* [34] proposed a setup to implement a higher-order exceptional surface with microring cavities that, at first glance, looks similar to our proposed schemes. However, our schemes offer two main advantages. (i) The asymmetric backscattering is induced globally as it comes from a single mirror at one WG, whereas in Ref. [34] at each cavity an auxiliary WG element for the asymmetric backscattering is placed. (ii) In Ref. [34], the position of the auxiliary WG elements needs to be tuned for the backscattering to be fully asymmetric. In contrast, our setups are rather robust against the exact position of the mirror. Further note that the authors of Ref. [34] focused on the lasing properties of the system, whereas the goal of this section is the frequency splitting and characteristic behavior of the mode pattern induced by an external perturbation to the system.

A. *N* Cavities Coupled to One WG with a Mirror

The setup for N microring cavities horizontally coupled via a single WG with a mirror is shown in Fig. 6(a). For the simulation of the system, we use the same parameters as in Section 2. The mirror is realized with a slit of gold with refractive index $n = 0.5 + 10i$. The slit has a width $w = h_{wg}/2$ and is placed $l = 1.2R$ right to the center of the most right cavity and introduces a backscattering coefficient R_m. By simulating a TP at the most left cavity in the respective N-cavity setup, the characteristic $2N$th root scaling of the frequency splitting at an EP_{2N} can be observed in Fig. 6.

Exemplary, the three-ring setup is considered. The effective Hamiltonian in the basis of CCW and CW waves in each microring is constructed as

(a)

4-ring setup 3-ring setup 2-ring setup 1-ring setup

(b)

$\Delta\Omega$

○ 1 ring $R_m = 0$
● 1 ring - EP_2
◆ 2 ring - EP_4
▲ 3 ring - EP_6
● 4 ring - EP_8

$\epsilon = (r_{TP}/R)^2$

Fig. 6. (a) Illustration of the setup with N microring cavities coupled to one semi-infinite WG with a mirror at the right-hand side. (b) The frequency splitting $\Delta\Omega$ due to a TP with radius r_{TP} at the leftmost cavity is shown. As a guide to the eye the scaling with $\sim\epsilon^\alpha$ is shown from bottom to top for (solid) $\alpha = 1$, (double dashed–dotted) $\alpha = 1/2$, (dotted) $\alpha = 1/4$, (dashed–dotted) $\alpha = 1/6$, and (dashed–double dotted) $\alpha = 1/8$.

$$H_0 = \begin{pmatrix} \Omega & D & A & 0 & 0 & 0 \\ D & \Omega & 0 & 0 & 0 & 0 \\ 0 & 0 & \Omega & D & A & 0 \\ 0 & A & D & \Omega & 0 & 0 \\ 0 & 0 & 0 & 0 & \Omega & D + R_m \\ 0 & 0 & 0 & A & D & \Omega \end{pmatrix}, \quad (10)$$

where it is assumed that a cavity couples solely to its neighbor. The coupling to the next but one cavity can be neglected. This assumption is valid, e.g., under critical coupling. For the ideal case $D = 0$, the effective Hamiltonian has one eigenvalue Ω and a single eigenvector $(1,0,0,0,0,0)^T$ indicating an EP_6 with a pure CCW eigenstate in the leftmost microring. The role of the mirror-induced asymmetric backscattering can be seen even more obviously by reordering the traveling-wave basis such that the first three components are the CCW waves in cavities 1, 2, and 3, and the second three entries represent CW waves in cavities 3, 2, and 1; the cavities are counted from left to right. Then the effective Hamiltonian assuming $D = 0$ reads

$$H_0 = \begin{pmatrix} \Omega & A & 0 & 0 & 0 & 0 \\ 0 & \Omega & A & 0 & 0 & 0 \\ 0 & 0 & \Omega & R_m & 0 & 0 \\ 0 & 0 & 0 & \Omega & A & 0 \\ 0 & 0 & 0 & 0 & \Omega & A \\ 0 & 0 & 0 & 0 & 0 & \Omega \end{pmatrix}, \quad (11)$$

which for any $R_m \neq 0$ represents an EP_6. It also shows that the system without a mirror at the WG has two EP_3 but is arbitrarily close to the EP_6. The structure of H_0 in Eq. (11) is similar to the structure of the Jordan normal form and appears also in the context of the Hatano–Nelson model of a cylindrical superconductor [42], where it can be understood as the nonperiodic, fully asymmetric limiting case [25].

The formation of the EP_6 is confirmed by FEM simulations of the dielectric structure as shown in Fig. 7 where the mode pattern of one of the calculated modes is presented. A difference to the other five mode patterns cannot be observed by eyes (not shown) due to the extreme non-orthogonality.

For single-particle sensing, three cases can be distinguished. The TP can be placed from left to right at cavity 1, 2, or 3 as indicated by the symbols in Fig. 8(a). These three cases lead to a different perturbation matrix $H_{TP}^{(1)}(\epsilon) = H_{TP}(\epsilon) \oplus 0_{4,4}$, $H_{TP}^{(2)}(\epsilon) = 0_{2,2} \oplus H_{TP}(\epsilon) \oplus 0_{2,2}$, or $H_{TP}^{(3)}(\epsilon) = 0_{4,4} \oplus H_{TP}(\epsilon)$ [in the basis used in Eq. (10)]. In the parameter space, these three cases represent selected perturbation direction, which in

gold mirror

Fig. 7. Mode pattern $|\psi|$ at the EP_6 for 3 microring cavities coupled to one WG with a gold mirror at the right side. Red arrows indicate the propagation direction of the field.
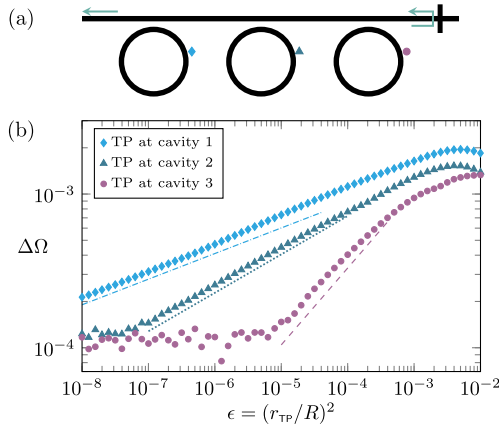
Fig. 8. (a) Illustration of three microring cavities coupled to one semi-infinite WG with a gold mirror at the end. The position of a TP is indicated by colored symbols. (b) The frequency splitting $\Delta\Omega$ due to a TP with radius r_{TP} at cavity 1, 2, or 3 is shown by dots. As a guide to the eye, the scaling with $\sim\epsilon^\alpha$ is shown from bottom to top for (dashed) $\alpha = 1/2$, (dotted) $\alpha = 1/4$, and (dashed–dotted) $\alpha = 1/6$.

the ideal case of $D = 0$ results in a frequency splitting according to $\sim\epsilon^{1/6}$, $\sim\epsilon^{1/4}$, and $\sim\epsilon^{1/2}$, respectively. This cavity-selective scaling of the splitting is confirmed by FEM simulations of the dielectric structure as shown in Fig. 8(b).

B. N Cavities Coupled via $N + 1$ WGs

The second setup to generate an EP of order $2N$ utilizes N vertically arranged cavities that are coupled via $N + 1$ WGs; see Fig. 9(a). The most upper WG has a mirror at a specific end that induces an asymmetric backscattering between CW and CCW waves in the adjacent cavity. The most lower WG is placed to have the same WG-induced internal backscattering for each of the cavities. To verify the respective order of the EP, a TP at the most lower cavity is placed. As shown in Fig. 9(b) systematically, the expected scaling of the frequency splitting can be observed for a variation of the TP radius. In addition, a cavity-selective scaling of the frequency splitting is shown in Fig. 9(c) for a four-ring setup.

The effective Hamiltonian describing the four-ring setup in the basis of CCW and CW waves from the lowest to the upper cavity reads

$$H_0 = \begin{pmatrix} \Omega & D & 0 & 0 & 0 & 0 & 0 & 0 \\ D & \Omega & A & 0 & 0 & 0 & 0 & 0 \\ 0 & 0 & \Omega & D & 0 & A & 0 & 0 \\ A & 0 & D & \Omega & 0 & 0 & 0 & 0 \\ 0 & 0 & 0 & A & \Omega & D & 0 & 0 \\ 0 & 0 & 0 & 0 & D & \Omega & A & 0 \\ 0 & 0 & 0 & 0 & 0 & 0 & \Omega & D + R_m \\ 0 & 0 & 0 & 0 & A & 0 & D & \Omega \end{pmatrix}. \quad (12)$$

For $D = 0$, the Hamiltonian is at an EP_8 with eigenvalue Ω and eigenvector $(0, 1, 0, 0, 0, 0, 0, 0)$ that represents a pure CW wave in the bottom-most cavity. This can be seen well in the FEM simulations in Fig. 10. Progressing to a finite $D \approx 10^{-10}(-11.4803 - 4.3397i)$, $\Omega \approx 8.3132 - 6.9647 \times 10^{-4}i$,
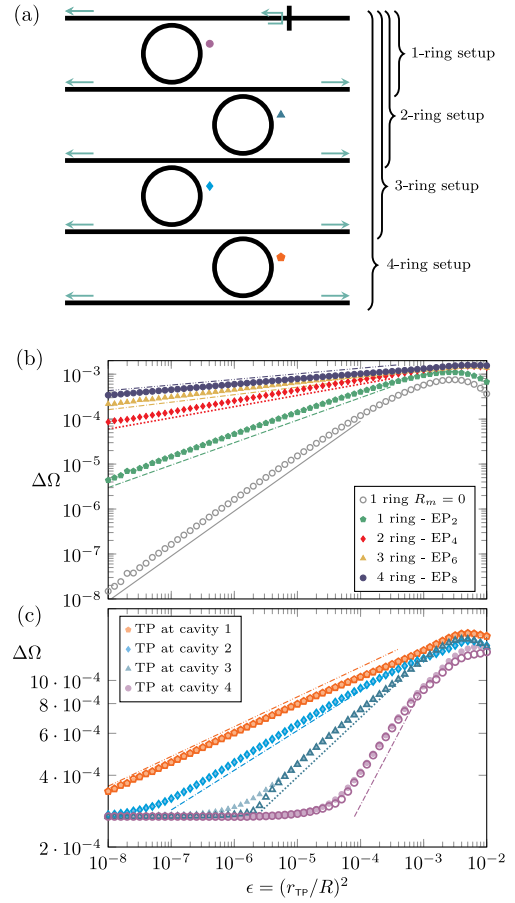

Fig. 9. (a) Illustration of four WG-coupled microring cavities. The WGs are infinitely long without backscattering except for the most upper WG that has a mirror at one end. (b) The frequency splitting $\Delta\Omega$ due to a TP with radius r_{TP} at the most lower cavity is shown. (c) For a four-microring setup the splitting $\Delta\Omega$ due to a TP at cavity 1, 2, 3, or 4 (from bottom to top) is shown. Filled symbols are results from the FEM simulation. The corresponding open symbols are calculated from the effective Hamiltonian. The lines in (b) and (c) serve as guides to the eye and represent the scaling $\sim\epsilon^\alpha$ with (solid) $\alpha = 1$, (double dashed–dotted) $\alpha = 1/2$, (dotted) $\alpha = 1/4$, (dashed–dotted) $\alpha = 1/6$, and (dashed–double dotted) $\alpha = 1/8$.

and $(A, R_m) \approx 10^{-4}(-2.44547 - 6.6842i, -1.2194 + 6.2931i)$ (see Appendix B) allows us to capture the correct splitting including the cavity-selective sensing with $\epsilon^{1/8}$, $\epsilon^{1/6}$, $\epsilon^{1/4}$, or $\epsilon^{1/2}$ for a TP at cavity 1, 2, 3, or 4 (from bottom to top respectively); see Fig. 9(c).

Next, the behavior of the mode patterns for a TP perturbation at a given cavity is analyzed. Therefore, the intensity for each of the eight mode patterns g in the cavity f is calculated numerically by integrating the mode pattern. Additionally, performing an average over the eight modes gives the averaged intensity I_f in cavity f as

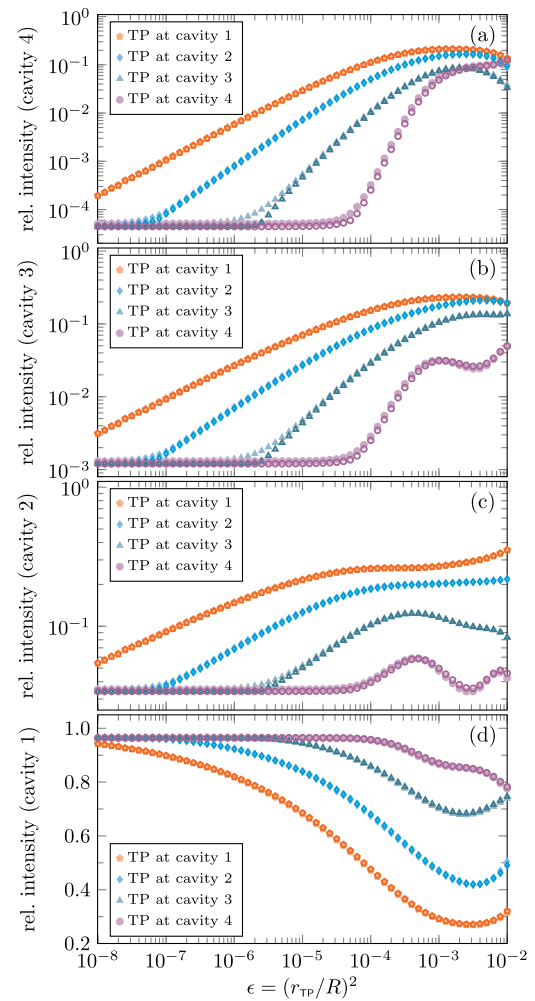$$I_f = \frac{1}{8}\sum_{g=1}^{8}\int_{\text{cavity } f}|\psi_g(x, y)|^2 dx dy. \quad (13)$$

The intensities I_f are then normalized to give relative intensities, i.e., $\sum_{f=1}^{4}I_f = 1$. The behavior of these relative
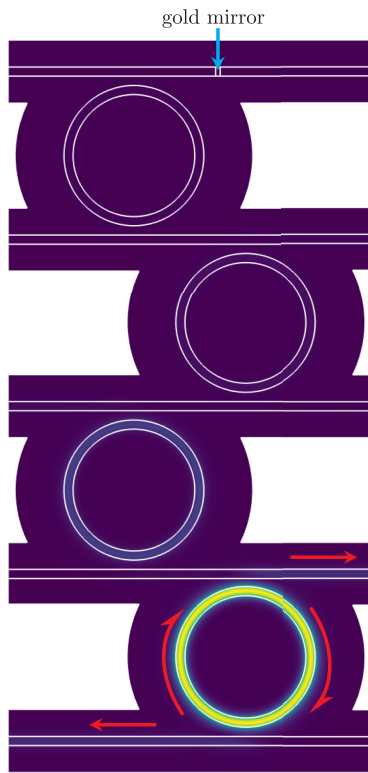
Fig. 10. Mode pattern $|\psi|$ at the EP_8 for four microring cavities coupled via WGs and a gold mirror. Red arrows indicate the propagation direction of the field.


Fig. 11. Relative intensity in each microring averaged over the eight modes in a four-ring setup perturbed by a TP is shown. The cavities are counted from bottom to top [(d) to (a)] in correspondence to the cavity position in Fig. 10. Filled symbols are results from the FEM simulation for a TP at a given cavity. The corresponding open symbols are calculated from the effective Hamiltonian.

intensities is shown in Fig. 11 for a variation of the TP radius and a perturbation of each cavity. For very small TP radii, the intensities converge to the mode pattern at the EP_8 (see Fig. 10), where (almost) all intensity accumulates in cavity 1. Increasing the TP radius leads to an exponential redistribution of the intensity. In cavities 2, 3, and 4, it exponentially increases with the perturbation strength while the relative intensity in cavity 1 decreases. The exponent of the exponential redistribution depends on the cavity where the TP is placed. Calculating the relative intensities from the effective Hamiltonian by analyzing its eigenvectors gives again an excellent agreement to the FEM simulations.

In practice, the position at which a TP interacts with a given cavity might not be controlled precisely. Therefore, Fig. 12 shows the eigenfrequency trajectories for a two-ring and four-ring setup if the angle ϕ_{TP} of the TP is varied. Since the azimuthal mode number is $m = 20$, a variation of ϕ_{TP} from $\pi/2$ to $\pi/2 - \pi/m$ represents a nearly periodic perturbation leading to a characteristic cyclic rotation of the $2N$ eigenfrequencies in complex plane, which is referred to as chirality of an EP_{2N} [43,44]. For larger TP radii, the eigenfrequency trajectories get deformed until eventually one or two frequencies split and form their individual cyclic behavior in the complex plane. Although such a behavior is a change in the topology of the eigenfrequency trajectories, it is very well described by the effective Hamiltonian (see Fig. 12). Consistently with the sensitivity at a higher-order EP, the separation of such

an eigenfrequency trajectory happens for the four-ring setup at smaller TP radii as for the two-ring setup [cf. $r_{TP} = 0.06R$ in Fig. 12(e) and $r_{TP} = 0.12R$ in Fig. 12(j)].

Additionally, the effective Hamiltonian allows for a calculation of the reflection spectra if the system is excited with a (real-valued) frequency ω at a WG [26,45,46]. To do so, the effective Green's function,

$$G(\omega) = (\omega \mathbf{1} - H)^{-1}, \qquad (14)$$

is calculated, where $H = H_0 + H_{TP}^{(1)}$ is given as a $2N \times 2N$ matrix with H_0 for the system of the N WG-coupled cavities [see Eq. (12)] and $H_{TP}^{(1)}$ represents the perturbation by the TP at the bottom-most cavity (cf. Appendix B). Consequently, also the Green's function is given as a matrix of the same dimensions as the effective Hamiltonian H. For the reflection spectra, we consider a monochromatic wave with frequency ω entering from the left side of the bottom-most WG. Such a wave couples to the adjacent first cavity exciting a CCW wave. In the
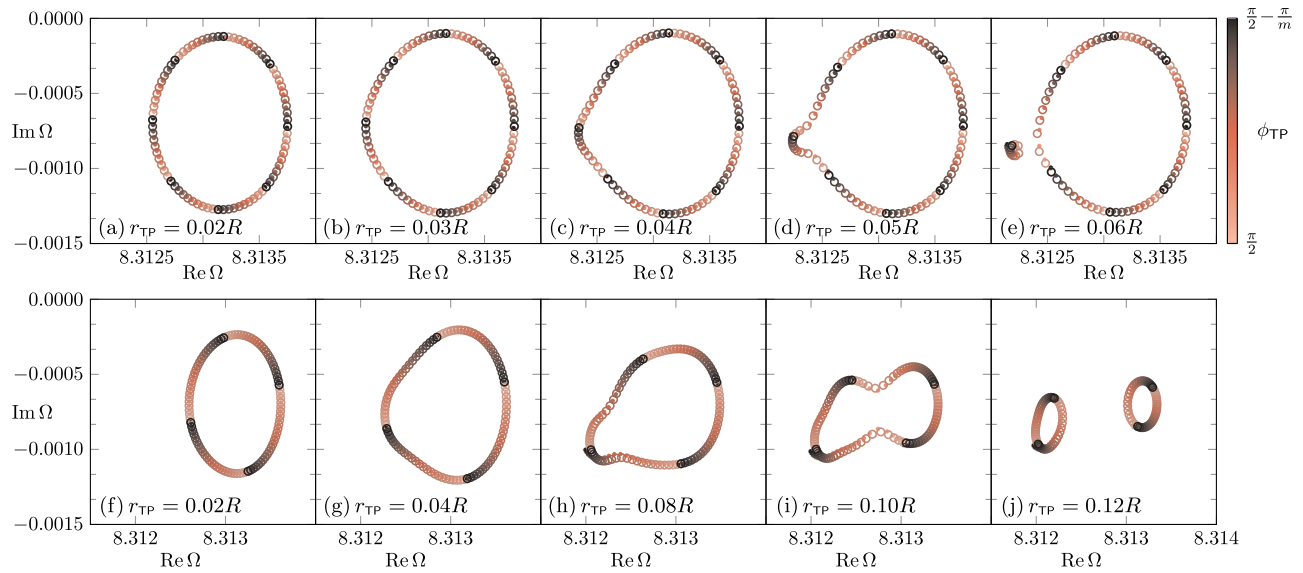
Fig. 12. Eigenfrequencies in complex plane for (a)–(e) four-ring and (f)–(j) two-ring setups [see Fig. 9(a)]. The color represents a variation of the TP angle ϕ_{TP} from $\pi/2$ to $\pi/2 - \pi/m$ with $m = 20$ being the azimuthal mode number. The TP is placed at the most lower cavity. From left to right the radius of the TP is increased. Filled dots are results from the FEM simulations. Open circles are calculated from the effective Hamiltonian. The markers lie nearly on top of each other.

traveling-wave basis, the excitation is, therefore, described by a vector with only one nonzero element in the first component. On the other hand, the light that leads to the reflected intensity in the most lower WG comes from the CW propagating wave in the first cavity, which is described by the second component of a vector in the traveling-wave basis. The matrix element G_{21} of the Green's function connects the CCW waves to the CW waves in the most lower cavity. Thus, the reflection spectra are obtained as [26]

$$R(\omega) = |G_{21}(\omega)A|^2. \tag{15}$$

In Fig. 13, it is demonstrated that the reflection spectra from Eq. (15) are in a very good agreement with the FEM simulations for a four-ring setup and a two-ring setup and different positions ϕ_{TP} of the TP.

Depending on the TP position ϕ_{TP}, individual peaks can be seen in the four-ring setup in Fig. 13(b) compared to a broad peak in the two-ring setup in Fig. 13(a). The reason is that the four-ring setup supports narrow peaks for the modes, whereas in the two-ring setup, the peaks associated with the modes are more broad and, therefore, overlap. Note that in order to separate the peaks of individual modes, it is also possible to add gain to the microrings. This typically results in more narrow peaks of the associated modes such that the modes can be distinguished in the spectrum.

However, narrowing of the peaks in the spectrum can already be seen in the passive systems without TP as shown in Fig. 14 (cf. [24,47]). The peaks in the reflection spectra are described by powers of a Lorentz curve $L(\omega) \sim |\omega - \Omega_{EP}|^{-2}$. Each additional cavity increases the order of the EP by 2, which gives an additional term of order $2N$ in the Green's function at the EP_{2N} [1,25,48],
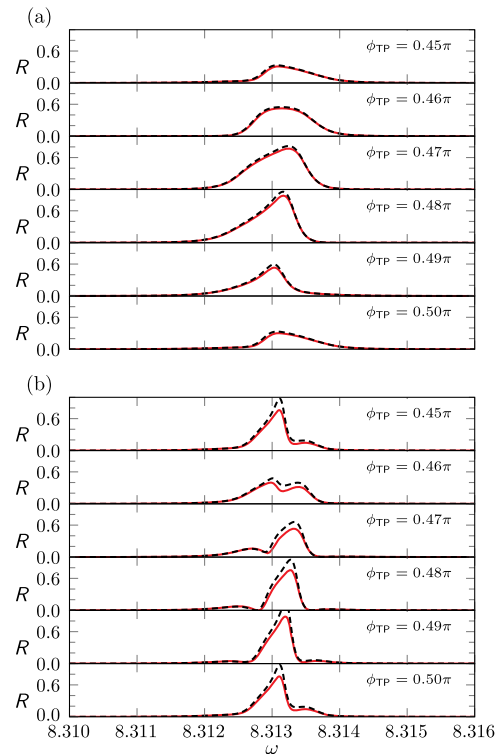
Fig. 13. Reflection spectra $R(\omega)$ for the (a) two-ring and the (b) four-ring setups are shown [see Fig. 9(a)], with a TP at the respective most lower cavity. The angle ϕ_{TP} is varied from $\pi/2$ to $\pi/2 - \pi/m$ with $m = 20$. The TP has a radius $r_{TP} = 0.03R$. Solid curves are the full numerical results and dashed curves are computed with the effective Hamiltonian.
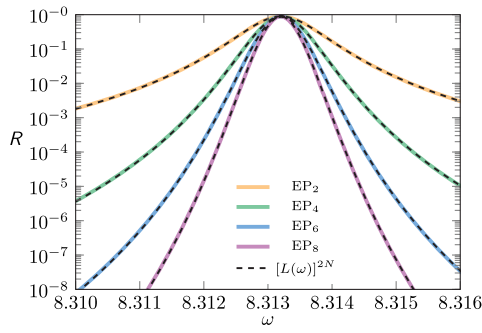
Fig. 14. Reflection spectra $R(\omega)$ for a setup with N microring cavities at an EP_{2N} [see Fig. 9(a)]. Colored curves are results from full numerical simulations. Dashed curves represent a fit with the $2N$ powers of the function $L(\omega) \sim |\omega - \Omega_{\mathrm{EP}}|^{-2}$.

$$G(\omega) = \sum_{k=1}^{2N} \frac{M_{k-1}}{(\omega - \Omega_{\mathrm{EP}})^k}, \tag{16}$$

where $M_0 = 1$ and $M_k = (H_0 - \Omega_{\mathrm{EP}}\mathbf{1})^k$ for $k \geq 1$. Thus, the reflection peaks in the N-ring setup are described by $R(\omega) \sim [L(\omega)]^{2N}$. Consequently, the four-ring setup shows more narrow peaks than the two-ring setup, which are then more likely to be separated rather than overlapping for a given perturbation. Note that the exponent $2N$ of the Lorentzian response is the same as the order of the EP if the effective excitation $|p\rangle$ is generic, i.e., $M_{2N-1}|p\rangle \neq 0$ [25]. The line shape might differ for non-generic excitation and different output channels [41].

4. SUMMARY

In this paper, we demonstrated two schemes for a handy and robust implementation of higher-order EPs with WG-coupled microring cavities. To do so, we synergized two approaches, namely the directional coupling of cavities via a WG [32] and the induced asymmetric backscattering from a mirror at the WG [35]. Thus, in a system of N cavities, an EP of order $2N$ is realized without complicated fine-tuned parameters. The order of the EP is verified by TP sensing. It is remarkable that the sensitivity is cavity-selective. Therefore, the induced frequency splitting not only depends on the perturbation strength, i.e., the size of the TP, but also on the cavity at which it interacts with the system. Conclusively, the WG-coupled microcavities are ideal systems to implement and study non-generic perturbations at higher-order EPs. An effective Hamiltonian based on coupled-mode theory is used to motivate the formation of the EPs as well as the sensing properties of the systems including the reflection spectra. Therefore, the effective Hamiltonian approach has been proven as an intuitive and insightful description of such systems at an EP of second or higher order.

A topic controversy discussed in recent literature is the signal-to-noise ratio of EP-based sensors. Some works indicate no enhancement of the signal-to-noise ratio at EPs [49–52], whereas others clearly show an enhancement [15,53]. Our proposed setup might be interesting for future studies on this topic

due to its simplicity and versatility to perform measurements at different WG ports.

Furthermore, recent works such as Ref. [34] show an increasing interest for the use of EP and exceptional surface physics in photonic devices. Recently employed experimental platforms range from rather conventional InGaAsP single and multiple quantum wells [18,54,55] to erbium ions [10], polymers [56], and perovskites [34], underlining the timeliness and versatility of EP photonics.

APPENDIX A: PARAMETERS OF THE PERTURBATION MATRIX

This section describes the process of determining the parameters U and V from the perturbation matrix H_{TP} in Eq. (2). The basic idea is to compare the numerically determined eigenvalues of an unperturbed system consisting of a microring and one or two WGs with the perturbed system, which includes additionally a TP of radius r_{TP} placed at an angle $\phi_{\mathrm{TP}} = \pi/2$. For the azimuthal mode number $m = 20$ and the before-mentioned choice of ϕ_{TP}, the matrix H_{TP} in Eq. (2) is simplified because $e^{\pm i2m\phi_{\mathrm{TP}}} = 1$. Within the framework of the coupled-mode theory, the effective Hamiltonian of the perturbed system in the traveling-wave basis reads as

$$H = H_0 + H_{\mathrm{TP}}(\phi_{\mathrm{TP}} = \pi/2), \tag{A1}$$

where the matrix H_0 in Eq. (1) describes the effective Hamiltonian of the unperturbed system. The structure of H and H_0 is equal for $\phi_{\mathrm{TP}} = \pi/2$. Therefore, they have the same eigenbasis, namely the standing-wave basis. The matrix

$$M^\dagger = \frac{1}{\sqrt{2}} \begin{pmatrix} 1 & 1 \\ i & -i \end{pmatrix} \tag{A2}$$

maps from the traveling-wave basis into the standing-wave basis. By taking the difference

$$\tilde{H} - \tilde{H}_0 = \tilde{H}_{\mathrm{TP}} = \begin{pmatrix} 2V & 0 \\ 0 & 2U \end{pmatrix}, \tag{A3}$$

where $\tilde{H} = M^\dagger H M$, $\tilde{H}_0 = M^\dagger H_0 M$, and $\tilde{H}_{\mathrm{TP}} = M^\dagger H_{\mathrm{TP}} M$, we can connect this result to the numerical simulations. Hence,

$$V = \frac{1}{2}(\Omega_{\mathrm{TP},1}^{\mathrm{num}} - \Omega_1^{\mathrm{num}}), \quad U = \frac{1}{2}(\Omega_{\mathrm{TP},2}^{\mathrm{num}} - \Omega_2^{\mathrm{num}}), \tag{A4}$$

where $\Omega_{\mathrm{TP},1,2}^{\mathrm{num}}$ are the numerically determined eigenvalues of the perturbed and $\Omega_{1,2}^{\mathrm{num}}$ of the unperturbed system.

In relation to the matrix $H_{\mathrm{TP}}(\epsilon)$ in Eq. (3), it is said that for small perturbations arising from a TP with radius r_{TP}, the perturbation parameter ϵ should scale with r_{TP}^2. This behavior is illustrated in Fig. 15 where the parameters V and U are determined with Eq. (A4). For small r_{TP}, the parameter U is orders of magnitude smaller than V; therefore, U is negligible in the matrix H_{TP} in Eq. (2). The scaling of V for small r_{TP} follows relatively close the r_{TP}^2 behavior and, therefore, also the perturbation parameter ϵ.
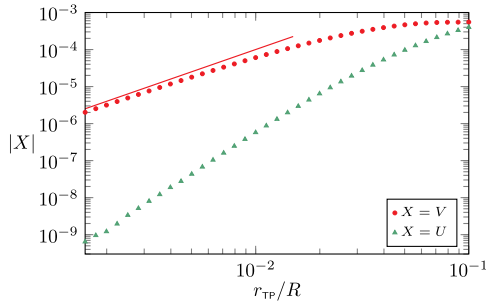
Fig. 15. Absolute values of the parameters V and U from the perturbation matrix with respect to radius r_{TP} of the TP. The line serves as a guide to the eye and represents the scaling proportional to r_{TP}^2.

APPENDIX B: PARAMETERS OF THE EFFECTIVE HAMILTONIAN

In order to determine the parameters Ω, A, R_m, and D for the effective Hamiltonian in Eq. (12), the difference between the eigenvalues of different effective Hamiltonians and the corresponding numerically determined eigenvalues is minimized under variation of the parameter subset.

The values of the parameters should be nearly independent from the number of microrings in the system because they model localized interactions between the traveling wave modes. Therefore, the two-ring setup [see Fig. 9(a)] is used to calculate the parameters. As a starting point, the system without a TP is chosen to determine Ω. The mean value of the four eigenvalues Ω_i^{num} with $i = 1, 2, 3, 4$ from the numerical simulation is set to

$$\Omega = \frac{1}{4} \sum_{i=1}^{4} \Omega_i^{\mathrm{num}}. \tag{B1}$$

With this choice of Ω, only the parameter subset $\chi = (A, R_m, D)$ has to be determined. For this purpose, the two-ring setups with a TP at the upper and a TP at the lower cavity are considered. We call them $\mathcal{S}^{(1)}$ and $\mathcal{S}^{(2)}$, respectively. These systems provide additional constraints for determining the parameter set χ. To get even more constraints, the TP radius r_{TP} is varied at a fixed TP position ϕ_{TP} for $\mathcal{S}^{(1)}$ and $\mathcal{S}^{(2)}$. For the effective Hamiltonian formalism, the variation of r_{TP} manifests itself as a variation from the parameters U and V. These perturbation parameters U and V are determined as described in Appendix A. All the previously mentioned constraints are parts of the set ζ. Each element ζ_i is related to $\mathcal{S}^{(1)}$ or $\mathcal{S}^{(2)}$ with a specific parameter configuration. The target function for the minimization reads as

$$f(\chi) = \sum_i \left(\min_{\{\sigma\}} \sum_\sigma \left| \Omega_j^{\mathrm{eff}}(\zeta_i, \chi) - \Omega_{\sigma(j)}^{\mathrm{num}}(\zeta_i) \right| \right), \tag{B2}$$

where the eigenvalues of the effective Hamiltonian with a specific parameter configuration are described through $\Omega_j^{\mathrm{eff}}(\zeta_i, \chi)$ and the corresponding eigenvalues of the numerical simulation are referred to as $\Omega_k^{\mathrm{num}}(\zeta_i)$. The $\{\sigma\}$ refers to the set of all permutations of the four eigenvalues $\Omega_k^{\mathrm{eff/num}}$ with $k = 1, 2, 3, 4$. The part with $\min_{\{\sigma\}}$ is needed because it is not clear which eigenvalue of the effective Hamiltonian should be compared with the numerical one. If too few constraints ζ_i are considered,

then it is possible to find parameters (A, R_m, D) that do not cover all numerically observed effects. For that reason, $\mathcal{S}^{(1)}$ and $\mathcal{S}^{(2)}$ are both part of the minimization process. It can be tricky to find well-suited start values $\chi_0 = (A_0, R_{m,0}, D_0)$ for the minimization of Eq. (B2). The expectation is $|D| \ll |A|$ and $|D| \ll |R_m|$. Hence, it can be beneficial to set $D = 0$ fixed and vary over (A, R_m) to get well-suited start values for the minimization over χ.

As mentioned in Section 2, the coupling parameter D between CW and CCW waves in a cavity describes more than the weak backscattering at the WG. In FEM simulations, artificial surface roughness arises intrinsically due to the finite size of the mesh elements. Also a finite simulation domain could influence D. It is recommended to use similar meshes and simulation domains for the minimization process to determine the parameter set (Ω, A, R_m, D).

Disclosures. The authors declare no conflicts of interest.

Data Availability. The data that support the findings of this study are available from the corresponding authors upon reasonable request.

REFERENCES

1. T. Kato, *Perturbation Theory for Linear Operators* (Springer, 1966).
2. M. V. Berry, "Physics of nonhermitian degeneracies," Czech. J. Phys. **54**, 1039–1047 (2004).
3. W. D. Heiss, "The physics of exceptional points," J. Phys. A Math. Theor. **45**, 444016 (2012).
4. H. Cao and J. Wiersig, "Dielectric microcavities: model systems for wave chaos and non-Hermitian physics," Rev. Mod. Phys. **87**, 61–111 (2015).
5. M.-A. Miri and A. Alù, "Exceptional points in optics and photonics," Science **363**, eaar7709 (2019).
6. E. J. Bergholtz, J. C. Budich, and F. K. Kunst, "Exceptional topology of non-Hermitian systems," Rev. Mod. Phys. **93**, 015005 (2021).
7. R. El-Ganainy, K. G. Makris, M. Khajavikhan, Z. H. Musslimani, S. Rotter, and D. N. Christodoulides, "Non-Hermitian physics and PT symmetry," Nat. Phys. **14**, 11–19 (2018).
8. J. Wiersig, "Chiral and nonorthogonal eigenstate pairs in open quantum systems with weak backscattering between counterpropagating traveling waves," Phys. Rev. A **89**, 012119 (2014).
9. J. Wiersig, "Sensors operating at exceptional points: general theory," Phys. Rev. A **93**, 033809 (2016).
10. W. Chen, Ş. K. Özdemir, G. Zhao, J. Wiersig, and L. Yang, "Exceptional points enhance sensing in an optical microcavity," Nature **548**, 192–196 (2017).
11. H. Hodaei, A. Hassan, S. Wittek, H. Carcia-Cracia, R. El-Ganainy, D. N. Christodoulides, and M. Khajavikhan, "Enhanced sensitivity at higher-order exceptional points," Nature **548**, 187–191 (2017).
12. Y.-H. Lai, Y.-K. Lu, M.-G. Suh, Z. Yuan, and K. Vahala, "Observation of the exceptional-point-enhanced Sagnac effect," Nature **576**, 65–69 (2019).

13. C. Zeng, Y. Sun, G. Li, Y. Li, H. Jiang, Y. Yang, and H. Chen, "Enhanced sensitivity at high-order exceptional points in a passive wireless sensing system," Opt. Express **27**, 27562–27572 (2019).

14. J. Wiersig, "Review of exceptional point-based sensors," Photonics Res. **8**, 1457–1467 (2020).

15. R. Kononchuk, J. Cai, F. Ellis, R. Thevamaran, and T. Kottos, "Exceptional-point-based accelerometers with enhanced signal-to-noise ratio," Nature **607**, 697–702 (2022).

16. B. Peng, Ş. K. Özdemir, S. Rotter, H. Yilmaz, M. Liertzer, F. Monfi, C. M. Bender, F. Nori, and L. Yang, "Loss-induced suppression and revival of lasing," Science **346**, 328–332 (2014).

17. P. Miao, Z. Zhang, J. Sun, W. Walasik, S. Longhi, N. M. Litchinitser, and L. Feng, "Orbital angular momentum microlaser," Science **353**, 464–467 (2016).

18. H. Hodaei, M.-A. Miri, M. Heinrich, D. N. Christodoulides, and M. Khajavikhan, "Parity-time–symmetric microring lasers," Science **346**, 975–978 (2014).

19. A. Stegmaier, S. Imhof, T. Helbig, T. Hofmann, C. H. Lee, M. Kremer, A. Fritzsche, T. Feichtner, S. Klembt, S. Höfling, I. Boettcher, I. C. Fulga, L. Ma, O. G. Schmidt, M. Greiter, T. Kiessling, A. Szameit, and R. Thomale, "Topological defect engineering and PT symmetry in non-Hermitian electrical circuits," Phys. Rev. Lett. **126**, 215302 (2021).

20. Y. Wang, Y. Ren, X. Luo, B. Li, Z. Chen, Z. Liu, F. Liu, Y. Cai, Y. Zhang, J. Liu, and F. Li, "Manipulating cavity photon dynamics by topologically curved space," Light Sci. Appl. **11**, 308 (2022).

21. Y.-K. Lu, P. Peng, Q.-T. Cao, D. Xu, J. Wiersig, Q. Gong, and Y.-F. Xiao, "Spontaneous *T*-symmetry breaking and exceptional points in cavity quantum electrodynamics systems," Sci. Bull. **63**, 1096–1100 (2018).

22. C. Wang, X. Jiang, G. Zhao, M. Zhang, C. W. Hsu, B. Peng, A. D. Stone, L. Jiang, and L. Yang, "Electromagnetically induced transparency at a chiral exceptional point," Nat. Phys. **16**, 334–340 (2020).

23. F. Zhang, Y. Feng, X. Chen, L. Ge, and W. Wan, "Synthetic anti-PT symmetry in a single microcavity," Phys. Rev. Lett. **124**, 053901 (2020).

24. Q. Zhong, Ş. K. Özdemir, A. Eisfeld, A. Metelmann, and R. El-Ganainy, "Exceptional-point-based optical amplifiers," Phys. Rev. Appl. **13**, 014070 (2020).

25. J. Wiersig, "Response strengths of open systems at exceptional points," Phys. Rev. Res. **4**, 023121 (2022).

26. J. Kullig and J. Wiersig, "High-order exceptional points of counterpropagating waves in weakly deformed microdisk cavities," Phys. Rev. A **100**, 043837 (2019).

27. H. Jing, Ş. K. Özdemir, H. Lü, and F. Nori, "High-order exceptional points in optomechanics," Sci. Rep. **7**, 3386 (2017).

28. W. Xiong, Z. Li, Y. Song, J. Chen, G.-Q. Zhang, and M. Wang, "Higher-order exceptional point in a pseudo-Hermitian cavity optomechanical system," Phys. Rev. A **104**, 063508 (2021).

29. S. Wang, B. Hou, W. Lu, Y. Chen, Z. Q. Zhang, and C. T. Chan, "Arbitrary order exceptional point induced by photonic spin–orbit interaction in coupled resonators," Nat. Commun. **10**, 832 (2019).

30. Q. Zhong, J. Kou, Ş. K. Özdemir, and R. El-Ganainy, "Hierarchical construction of higher-order exceptional points," Phys. Rev. Lett. **125**, 203602 (2020).

31. J. Wiersig, "Revisiting the hierarchical construction of higher-order exceptional points," Phys. Rev. A **106**, 063526 (2022).

32. X.-Y. Wang, F.-F. Wang, and X.-Y. Hu, "Waveguide-induced coalescence of exceptional points," Phys. Rev. A **101**, 053820 (2020).

33. H. Yang, X. Mao, G.-Q. Qin, M. Wang, H. Zhang, D. Ruan, and G.-L. Long, "Scalable higher-order exceptional surface with passive resonators," Opt. Lett. **46**, 4025–4028 (2021).

34. K. Liao, Y. Zhong, Z. Du, G. Liu, C. Li, X. Wu, C. Deng, C. Lu, X. Wang, C. T. Chan, Q. Song, S. Wang, X. Liu, X. Hu, and Q. Gong, "On-chip

integrated exceptional surface microlaser," Sci. Adv. **9**, eadf3470 (2023).

35. Q. Zhong, J. Ren, M. Khajavikhan, D. N. Christodoulides, Ş. K. Özdemir, and R. El-Ganainy, "Sensing with exceptional surfaces in order to combine sensitivity with robustness," Phys. Rev. Lett. **122**, 153902 (2019).

36. Q. Zhong, S. Nelson, Ş. K. Özdemir, and R. El-Ganainy, "Controlling directional absorption with chiral exceptional surfaces," Opt. Lett. **44**, 5242–5245 (2019).

37. G.-Q. Qin, R.-R. Xie, H. Zhang, Y.-Q. Hu, M. Wang, G.-Q. Li, H. Xu, F. Lei, D. Ruan, and G.-L. Long, "Experimental realization of sensitivity enhancement and suppression with exceptional surfaces," Laser Photonics Rev. **15**, 2000569 (2021).

38. J. Wiersig, "Non-Hermitian effects due to asymmetric backscattering of light in whispering-gallery microcavities," in *Parity-time Symmetry and Its Applications*, Springer tracts in modern physics, D. Christodoulides and J. Yang, eds. (Springer, 2018), Vol. **280**, pp. 155–184.

39. J. Wiersig, "Structure of whispering-gallery modes in optical microdisks perturbed by nanoparticles," Phys. Rev. A **84**, 063828 (2011).

40. https://www.comsol.com.

41. A. Hashemi, K. Busch, D. N. Christodoulides, Ş. K. Özdemir, and R. El-Ganainy, "Linear response theory of open systems with exceptional points," Nat. Commun. **13**, 3281 (2022).

42. N. Hatano and D. R. Nelson, "Localization transitions in non-Hermitian quantum mechanics," Phys. Rev. Lett. **77**, 570–573 (1996).

43. W. D. Heiss and H. L. Harney, "The chirality of exceptional points," Eur. Phys. J. D **17**, 149–151 (2001).

44. W. D. Heiss, "Chirality of wavefunctions for three coalescing levels," J. Phys. A Math. Theor. **41**, 244010 (2008).

45. T. J. Kippenberg, S. M. Spillane, and K. J. Vahala, "Modal coupling in traveling-wave resonators," Opt. Lett. **27**, 1669–1671 (2002).

46. C. Manolatou, M. J. Khan, S. Fan, P. R. Villeneuve, H. A. Haus, and J. D. Joannopoulos, "Coupling of modes analysis of resonant channel add-drop filters," IEEE J. Quantum Electron. **35**, 1322–1331 (1999).

47. M. Khanbekyan and J. Wiersig, "Decay suppression of spontaneous emission of a single emitter in a high-Q cavity at exceptional points," Phys. Rev. Res. **2**, 023375 (2020).

48. W. D. Heiss, "Green's functions at exceptional points," Int. J. Theor. Phys. **54**, 3954–3959 (2015).

49. H.-K. Lau and A. A. Clerk, "Fundamental limits and non-reciprocal approaches in non-Hermitian quantum sensing," Nat. Commun. **9**, 4320 (2018).

50. W. Langbein, "No exceptional precision of exceptional-point sensors," Phys. Rev. A **98**, 023805 (2018).

51. H. Wang, Y.-H. Lai, Z. Yuan, M.-G. Suh, and K. Vahala, "Petermann-factor sensitivity limit near an exceptional point in a Brillouin ring laser gyroscope," Nat. Commun. **11**, 1610 (2020).

52. C. Chen, L. Jin, and R.-B. Liu, "Sensitivity of parameter estimation near the exceptional point of a non-Hermitian system," New J. Phys. **21**, 083002 (2019).

53. M. Zhang, W. Sweeney, C. W. Hsu, L. Yang, A. D. Stone, and L. Jiang, "Quantum noise theory of exceptional point amplifying sensors," Phys. Rev. Lett. **123**, 180501 (2019).

54. L. Feng, Z. J. Wong, R.-M. Ma, Y. Wang, and X. Zhang, "Single-mode laser by parity-time symmetry breaking," Science **346**, 972–975 (2014).

55. Z.-Q. Yang, Z.-K. Shao, H.-Z. Chen, X.-R. Mao, and R.-M. Ma, "Spin-momentum-locked edge mode for topological vortex lasing," Phys. Rev. Lett. **125**, 013903 (2020).

56. D. Korn, M. Lauermann, S. Koeber, P. Appel, L. Alloatti, R. Palmer, P. Dumon, W. Freude, J. Leuthold, and C. Koos, "Lasing in silicon–organic hybrid waveguides," Nat. Commun. **7**, 10864 (2016).